Wear 476 (2021) 203678

Contents lists available at ScienceDirect

Wear

journal homepage: http://www.elsevier.com/locate/wear

On the role of grain size on slurry erosion behavior of a novel medium-carbon, low-alloy pipeline steel after induction hardening

Vahid Javaheri [a,*], Oskari Haiko [a], Saeed Sadeghpour [a], Kati Valtonen [b], Jukka Kömi [a], David Porter [a]

[a] Centre for Advanced Steels Research, Materials and Mechanical Engineering, University of Oulu, Finland
[b] Tampere Wear Center, Materials Science and Environmental Engineering, Tampere University, Finland

ARTICLE INFO

Keywords:
Wear testing
Steel
Slurry erosion
Pipeline
Prior austenite grain size
Electron microscopy

ABSTRACT

Grain refinement has been widely used to enhance the hardness and toughness properties of metallic materials. However, the effect of prior austenite grain refinement on the final martensitic microstructure and wear performance of steels is not yet fully understood. In this study, induction hardening treatment with heating rates in the range 50–500 °C/s to the peak temperatures of 900 and 1000 °C followed by water quenching has been employed to produce through-hardened microstructures in a new medium-carbon, low-alloy steel intended as a slurry transportation pipeline material. The results revealed that in the range of achieved prior austenite grain size i.e. 2-15 μm, during different heating paths, the final martensitic microstructures experienced only a slight difference in the size of blocks and level of hardness. The mean hardness, hardness homogeneity, and grain structure uniformity were highest with a heating rate of 50 °C/s, especially for those samples which were re-austenitized at the peak temperature of 900 °C. A pin-mill type of high-speed slurry-pot wear tester was used to evaluate the slurry erosion behavior of the steel. It was found that prior austenite grain size in the above-mentioned range had no significant effect on the final microstructure and hardness value, however, the slight difference in martensite block size did notably influence the work hardening behavior and consequently the wear mechanism of the samples during the tests.

1. Introduction

Steel pipelines have been considered as an effective means for the long-distance transportation of mining and cement slurry products. However, material removal from the pipeline surface by solid particles has been a major concern as it can cause extensive damage and high maintenance costs. Such a progressive loss of material under repeated impacts of fine and coarse solid particles is a process of wear called "slurry erosion". Despite some attempts [1–4], due to the slurry erosion complexity and several parameters involved, there is no universal model yet that can effectively estimate the erosion rate of materials, especially considering the role of the target material properties. Thus, to evaluate the slurry erosion behavior of new material for the erosion-resistant application, experimental assessment is still needed.

In the case of pipeline materials, erosion rate plays a decisive role in determining the pipe thickness and the system operating parameters. In a previous review paper [5], it was shown that there are several test rigs to evaluate the slurry erosion behavior of materials such as slurry pot test [6], jet erosion tester [3], Coriolis erosion tester [7], and closed-loop pipeline rig [8]. The slurry pot test would be one of the best in the case of the ranking of slurry erosion resistance, thanks to its simplicity, short duration, and inexpensive cost as well as producing comparatively realistic results for many fields of applications. Previous studies [5,9,10] showed that erosion is mainly affected by erosive particles size, shape, density, hardness, and impact angle and velocity as well as protective material characteristics.

In the case of slurry transportation pipeline, erosion becomes tougher as conditions are very harsh – aggressive impingement on the pipe wall by the traveling large solid particles causes severe damage. Clearly, when impacting the surface, larger particles accelerate the slurry erosion rate over that produced by smaller particles as they transfer more kinetic energy to the material surface and result in greater material removal per impact. Besides, in the case of high-speed particle impacts, impingement angle i.e. the angle between the impact direction

* Corresponding author.
E-mail address: vahid.javaheri@oulu.fi (V. Javaheri).

https://doi.org/10.1016/j.wear.2021.203678
Received 7 September 2020; Received in revised form 8 December 2020; Accepted 9 December 2020
Available online 11 February 2021

Table 1
Chemical composition of studied material (in wt.%).

Alloy	C	Si	Mn	Cr	Ni	Mo	Nb	N
Studied material	0.40	0.19	0.24	0.92	0.02	0.48	0.013	0.004
Ref X material	0.30	0.80	1.70	1.50	1.00	0.50	–	–

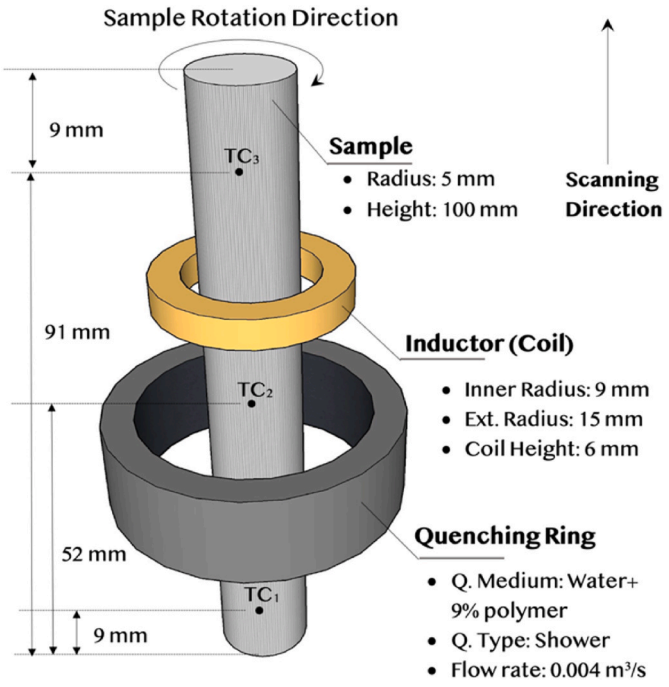

Fig. 1. Set up of induction hardening machine.

and target material surface is another key parameter affecting the erosion rate. Furthermore, the variation of total erosion depends on the target material properties. According to the previous studies which were carried out on various steel compositions [5,11], generally, slurry erosion is accomplished by two complementary mechanisms, namely the "deformation" mechanism which is associated with particle impingements normal to the eroded surface and the "cutting" mechanism which is associated with suspended particle impingements parallel to the eroded surface. In other words, the erosion mechanism is typically a combination of these two mechanisms, when particles attack the surface at various angles. However, despite several research works on the solid particle erosion of steel materials, to the best knowledge of authors, the role of steel microstructure on the slurry erosion behavior has not been well discussed as yet. For instance, it has been reported that prior austenite grain size (PAGS) had a marked effect on improving the strength and toughness of carbon steels [12–15], but the role of PAGS on the wear performance of martensitic steels is still not well understood. Martensitic steels might benefit from the refinement of PAGS in resisting high-stress abrasive wear [16], but generally, there are quite mixed results regarding the wear resistance and grain size of metallic materials [17]. Therefore, a great deal of effort is still required for a proper understanding of the relationship between microstructure and wear resistance of steels in slurry-erosive conditions. Hence, the current research work was established to investigate the effect of prior austenite grain size as well as final martensitic block size on the wear performance of a martensitic steel (medium carbon) in slurry erosive conditions.

2. Experimental procedure

2.1. Materials

The studied material in this work was an as-rolled bainitic medium-carbon, low-alloy steel which has been designed by the authors' team for possible application as a slurry transportation pipeline material. The steel chemistry is listed in Table 1 and more details on the composition design, as-rolled material properties, and induction hardening behavior can be found in previous publications [18–21]. Also, a commercial 500 HB grade wear-resistant steel was included as a reference material (Ref

Table 2
The samples' code according to their heat treatment condition.

Re-austenitization temperature (°C)	Nominal average heating rate (°C/s)			
	10	50	100	500
900	CHT	Fast-900	Super Fast-900	Ultra Fast-900
1000	–	Fast-1000	Super Fast-1000	Ultra Fast-1000

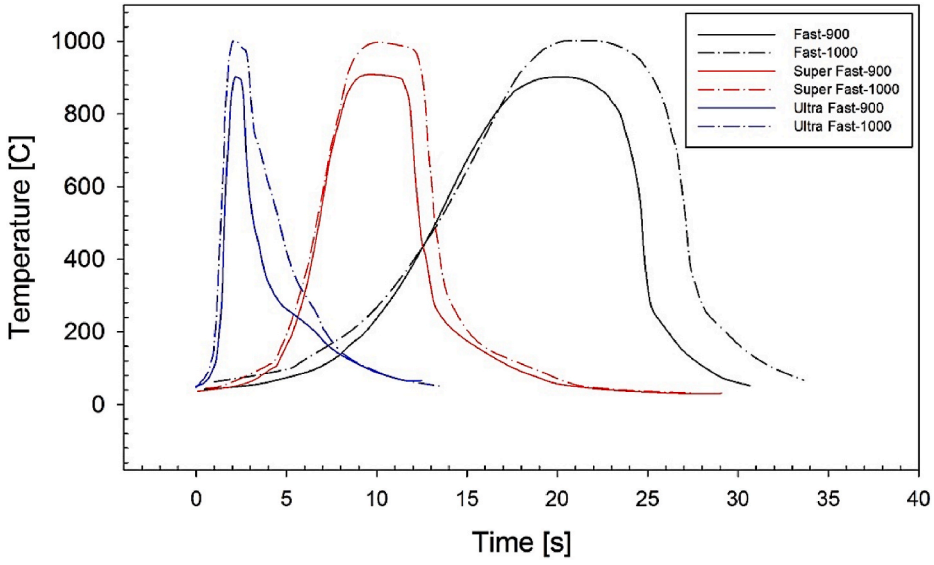

Fig. 2. Thermal paths of induction hardening treatments indicating the different applied heating rate and peak temperatures.

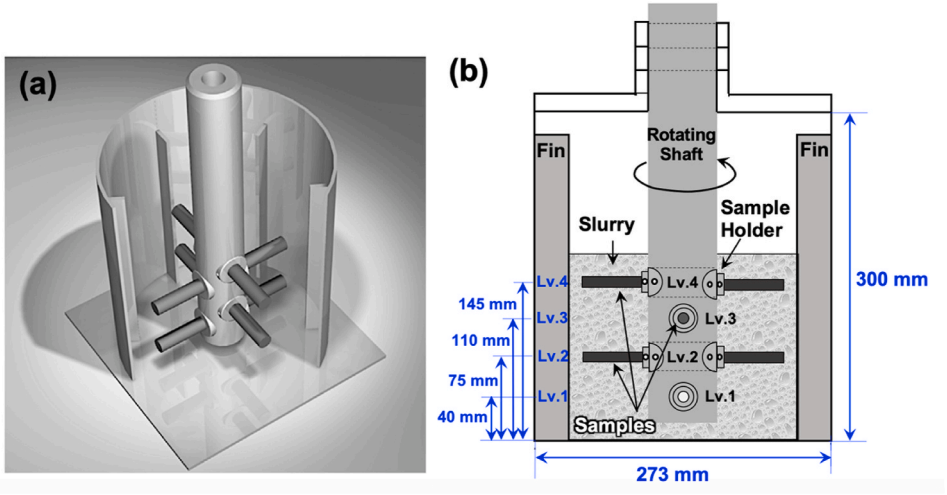

Fig. 3. High-speed slurry-pot set-up. a) a 3D schematic illustration [22] and b) detailed 2D illustration indicating the dimensions of the slurry-pot and sample holders position. Level 1 was not used during all the test batches.

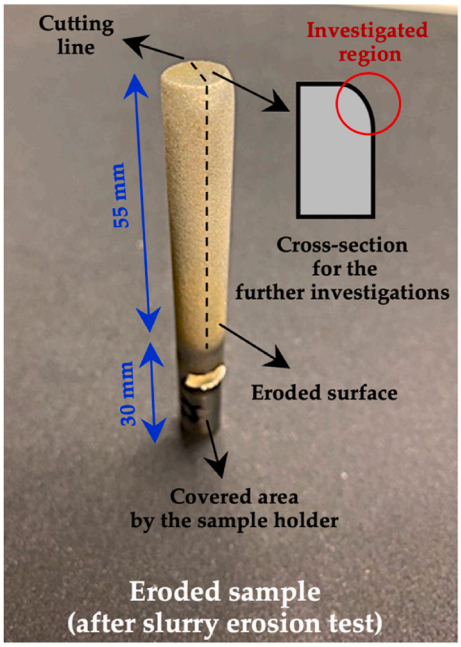

Fig. 4. An illustration of a sample after erosion test showing the position of the selected region for the detailed investigations.

X) in the wear testing.

2.2. Induction hardening

Induction hardening has been employed to produce very fine grain structures. For this purpose, cylindrical bar samples made from the as-rolled material were subjected to different thermal cycles using an industrial hardening machine. The device consists of adjustable heating and cooling systems. Fig. 1 shows a schematic illustration of the sample geometry and hardening machine setup including an inductor as a source of heat coaxial with a quenching ring as a source of cooling. To fabricate the different grain sizes, the heat was generated at different rates of around 50 °C/s, 100 °C/s, and 500°/s that here, for the sake of simplicity, are named as Fast, Super-fast, and Ultra-fast heating rates, respectively. A scanning induction method was applied to the samples, and in order to provide uniform heating through the whole sample, the

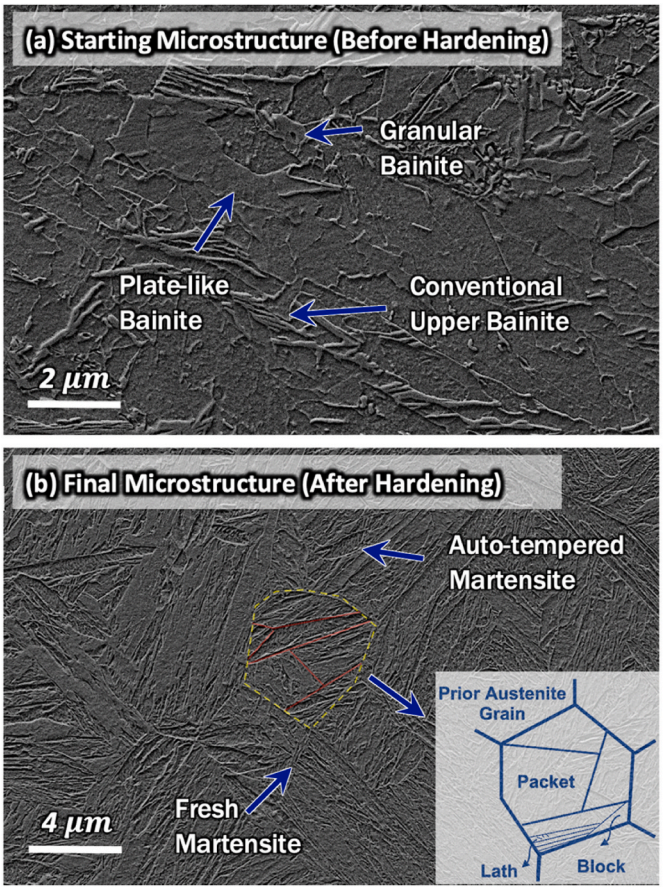

Fig. 5. SEM micrographs of the studied material indicating a) the as-rolled microstructure before induction hardening and b) the induction hardened microstructure of Fast-900 sample prior to the erosion test.

specimen was rotated around its axis. Two peak temperatures of 900 °C and 1000 °C were applied as the austenitization temperatures for each heating rate. In total, there were 6 different target cycles as shown in Fig. 2. Upon heating, depending on the heating rates, different dwell times with a maximum of 6 s were applied. Then, similar quenching for all samples was performed by spraying a mixture of water and 9% commercial AquaQuench 365 cooling medium at the rate of 0.4 L/s. To

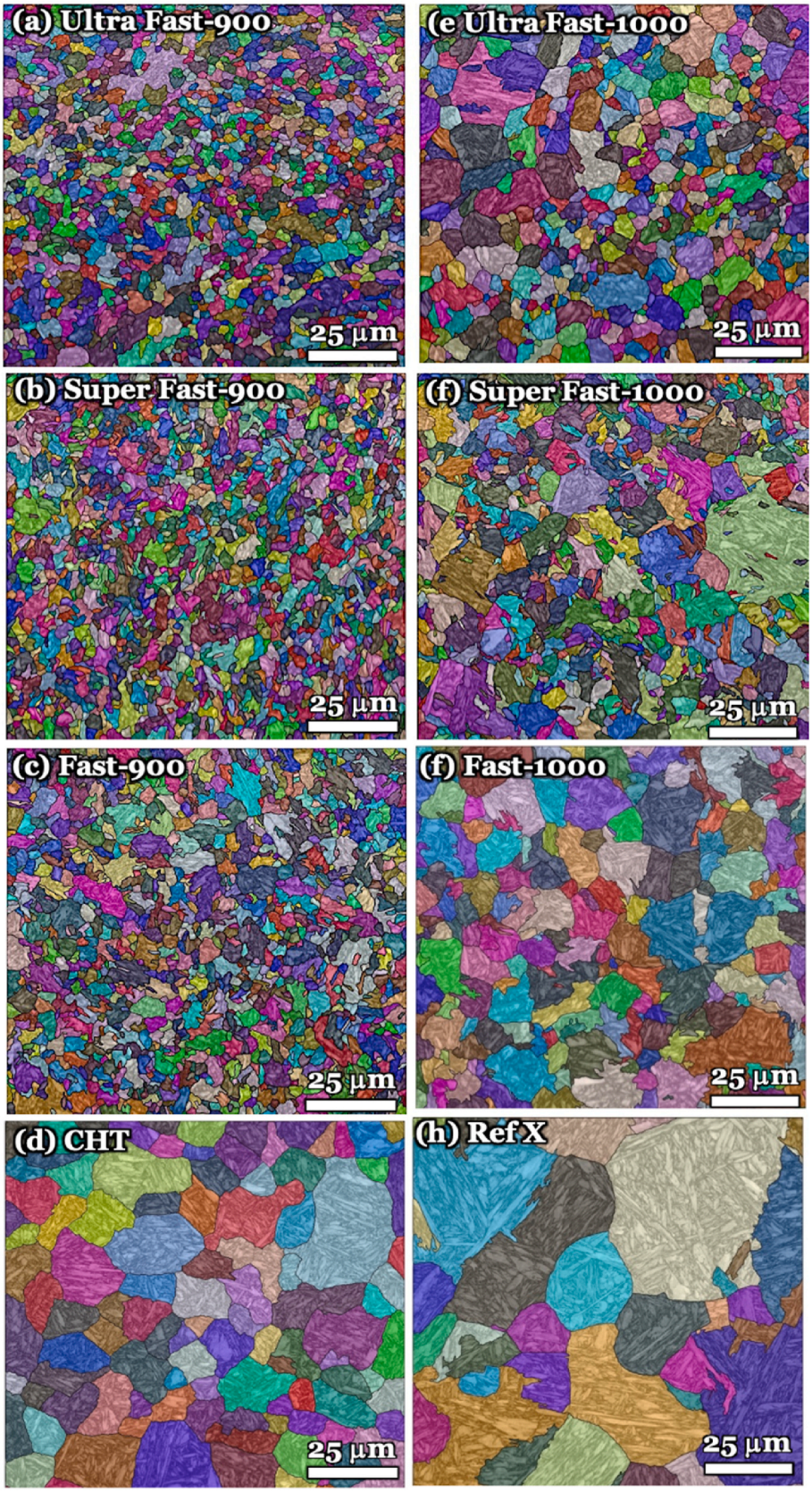

Fig. 6. The reconstructed prior austenite grain structures of a) Fast-900, b) Super Fast-900, c) Ultra Fast-900, d) CHT, e) Fast-1000, f) Super Fast-1000, g) Ultra Fast-1000 and h) Ref X.

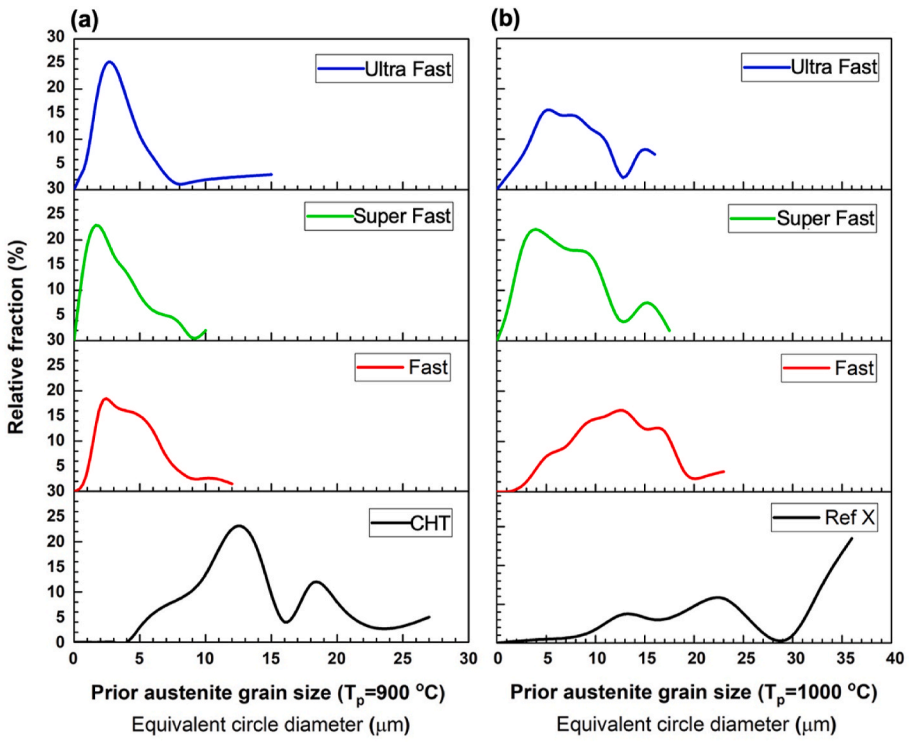

Fig. 7. Prior austenite grain size distribution of induction hardened samples with the peak temperature of a) 900 °C along with CHT sample and b) 1000 °C along with Ref X sample.

monitor the whole process and to be sure of uniform heating and cooling, three thermocouples were connected to the top, middle, and bottom of the samples and an average value is reported for each condition. Each condition was repeated twice to provide more samples for the slurry pot test and to reduce any probable test errors.

Besides the induction hardened samples, a conventionally heat-treated sample (CHT) and a well-known commercial quenched 500 HB grade (Ref X) wear-resistant steel were prepared to be tested as reference material in each slurry erosion test batch. The CHT sample was heated in an electric muffle furnace with a rate of 10 °C/s to 900 °C and then quenched in a water bath. The CHT sample along with the target samples were named according to their thermal history as listed in Table 2. Commercial reference sample, Ref X, is not included in the table as it was used with no further heat treatment.

2.3. Slurry erosion wear tests

To evaluate the slurry erosion performance in an accelerated manner, a pin-mill type high-speed slurry-pot test rig was employed [22]. The method has been utilized for the investigation of various materials in slurry-erosive conditions [22–25]. The device consists of a rotating main shaft with 2–8 test specimens embedded on four levels, which is mounted inside a cylindrical pot containing the slurry. A schematic illustration of the test setup is given in Fig. 3. Four fins have been fixed inside the pot in order to minimize the centrifuging of the fluid inside the pot as well as to prevent local erosive particle pile up and concentration on the pot wall. Six different round-bar type samples with a diameter of 9.5 mm and length of 85 mm (cut and machined from the induction hardened samples) were used in each test batch. Three test batches were performed in total.

A similar slurry mixture of 10 L of water and 2 kg of crushed and sieved Kuru granite particles with a particle size distribution of 10–12 mm was used in all tests. The average hardness value of the granite particles was about 1000 HV. The samples were spun in the pot at 1500 rpm for 180 min in total. The highest speed at the tip of the sample was about 13 m/s. For these tests, high slurry speed and large erosive particles were considered to simulate harsh slurry transportation conditions. Typically, in the slurry transportation applications, the concentration is low, down to 10–20 wt%, but particles are large, up to 50 mm and the transportation speeds are high, up to 30 m/s. To decrease the effect of particle degradation, after a time interval of 30 min, the slurry was replaced with a fresh one. In total, there were six intervals for each batch, and each time the sample position (level) was switched to provide similar erosive conditions for each sample, i.e. the sample which was first placed on the upper level for the first 30 min, was switched to the lower level for another 30 min and so on. The erosion was measured in each time interval using the mass loss technique with a microelectronic balance having a least count of 0.0001 g. Before weighing, the specimens were properly cleaned through a sequence of washing with tap water, rinsing in alcohol, and drying with hot air.

2.4. Microstructure characterization

Microstructural features of samples before and after induction hardening, as well as the eroded surfaces, were examined using a Field Emission Scanning Electron Microscope (FESEM, Zeiss Sigma) after a standard sample preparation method including cross-sectioning, grinding and polishing with 1 μ m diamond paste followed by nital etching (2%) to reveal the microstructure. Electron backscatter diffraction (EBSD) analyses were also performed on samples without etching and after one more chemical polishing step, and surface nickel coating was also applied for the EBSD samples in order to improve the surface conductivity. EBSD mappings were recorded using an accelerating voltage of 15 kV and a working distance of 15 mm with a step size of 0.1 μm. The examined region for both EBSD and SEM investigations was the tip of the samples, which was heavily damaged during the erosion, as shown in Fig. 4.

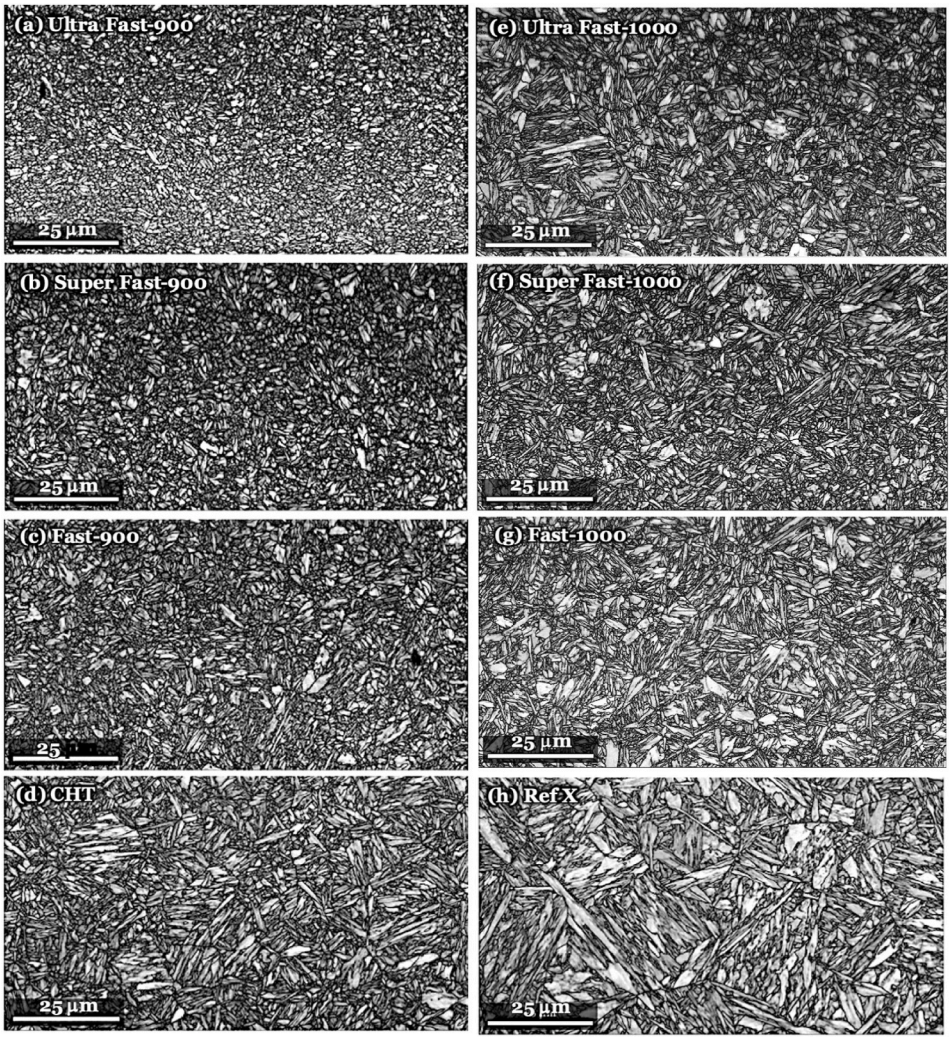

Fig. 8. The image quality maps of the samples prior to the erosion test for a) Fast-900, b) Super Fast-900, c) Ultra Fast-900, d) CHT, e) Fast-1000, f) Super Fast-1000, g) Ultra Fast-1000 and h) Ref X.

2.5. Prior austenite grain reconstruction

Initially, unsuccessful attempts were made to reveal the prior austenite grain structure using laser scanning confocal microscopy after etching with the common etchant for exposing prior austenite structure containing saturated aqueous picric acid solution along with a few drops of detergent and hydrochloric acid. Afterward, prior austenite grains were reconstructed with the aid of a computational method which was applied to the EBSD data using Matlab supplemented with the MTEX texture and crystallography analysis toolbox [26]. Briefly about the reconstruction technique, the process involved the initial assembly of ferritic grain maps from the data sets with a grain misorientation angle tolerance of 3–5° and the reconstruction algorithm on the basis of orientation relationship between the parent austenite and product ferritic phase using the relationship proposed Kurdjumov–Sachs (K–S) [27]. More details about the reconstruction technique can be found elsewhere [26,28].

2.6. Hardness measurements

The bulk hardness of the samples prior to the erosion tests was measured right after each thermal cycle using a Vickers Hardness Tester (Struers Duramin A-300) under 10 Kgf load and dwell time of 10 s. The hardness values are given as an average of at least five indentations per sample. After the slurry erosion test, the microhardness profiles from the region near the surface with the maximum mass removal (highlighted in Fig. 4) were provided by employing CSM Instruments MHT-Z-AE Vickers microhardness tester with 0.1 N load.

3. Results and discussion

3.1. Microstructures

The initial microstructure of the materials before induction hardening is presented in Fig. 5(a). The microstructures consisted of a mixture of different bainitic morphologies, including plate-like bainite, granular bainite, and conventional upper bainite, as marked in Fig. 5(a). A detailed description of the starting microstructure can be found elsewhere [19]. As expected, due to the high rate of cooling during the hardening process, the final microstructures of all samples after the induction hardening showed the typical characteristics of lath-type martensite, i.e. packets, blocks, sub-blocks, and lath structure. It is well-known that during martensite formation through quenching, the parent austenite grains break down into different packets so that each of them further subdivides to the several blocks and extended sub-blocks which contain numerous martensitic laths [29]. As an example, the microstructure of the Fast-900 sample is given in Fig. 5(b), indicating mainly freshly formed lath martensite as well as some partially auto-tempered martensitic regions.

In order to obtain additional insight into the microstructural details

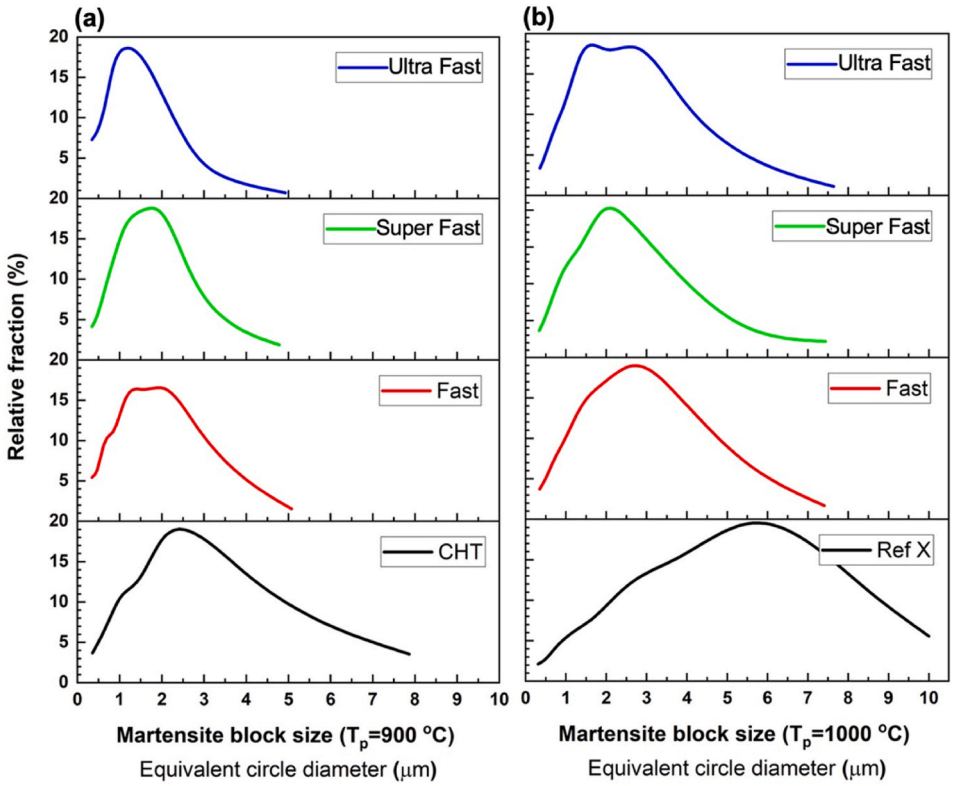

Fig. 9. Martensite blocks size distribution (represented by ECD) of induction hardened samples with the peak temperature of a) 900 °C along with CHT sample and b) 1000 °C along with Ref X sample.

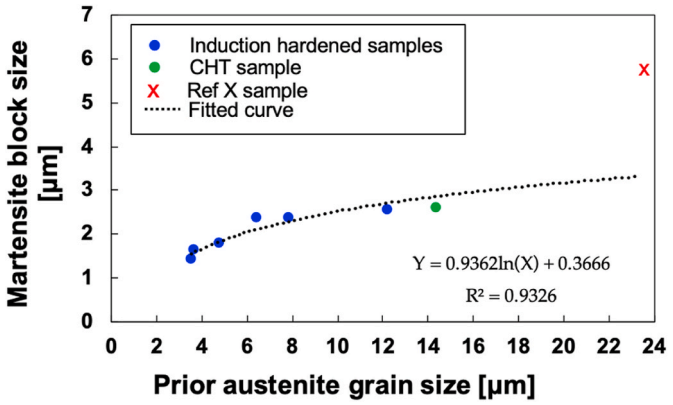

Fig. 10. The correlation between the prior austenite grain size and martensite block size, (mean ECD value). Due to its different composition, Ref X is not included in the fitting.

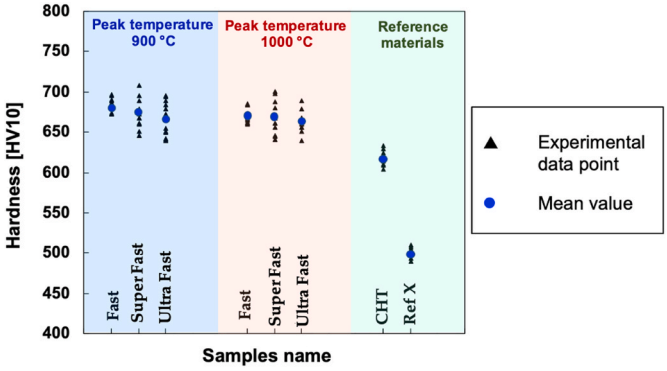

Fig. 11. The mean hardness value (HV 10) along with all the experimental data points for all the samples prior to the erosion testing indicating hardness inhomogeneities.

of the hardened samples, the features of the final microstructure were characterized using FESEM-EBSD. The EBSD data were used later utilized for the reconstruction of prior austenite grain structure. The reconstructed prior austenite grains of the studied samples as well as those of the reference materials are shown in Fig. 6. The relative distribution graphs of the prior austenite grain size, which are calculated as equivalent circle diameter (ECD), are presented in Fig. 7. For all the hardened samples irrespective of the heating rate, the elongated and pancake-shaped starting prior austenite structure observed in the as-rolled samples was completely eliminated after the re-austenitization and induction hardening. It was clearly observed that the higher heating rate and the lower peak temperature led to a finer prior austenite grain structure.

The image quality (IQ) maps of the final martensitic microstructures for all specimens are presented in Fig. 8. The blocks are very fine and almost equiaxed in the case of samples austenitized at 900 °C for all examined heating rates, while for those heated up to 1000 °C the blocks appear rather elongated and larger. The equivalent circle diameter of martensite blocks, which are the finest possible martensitic feature to be measured accurately via EBSD, was calculated considering the boundaries with a misorientation angle more than 15°, which in fact were mainly in the range 45–60°. The distribution graphs of martensite block size for all the samples are demonstrated in Fig. 9. Except for both of the reference materials, all the other samples showed a similar trend with an almost log-normal distribution and a peak ECD value around 1.5 μm for the samples austenitized at 900 °C and about 2.5 μm for those austenitized at 1000 °C. The samples Fast-900 and Fast-1000 showed the most uniformly distributed prior austenite grains as well as martensite blocks. However, the finest and the most equiaxed structure was achieved for

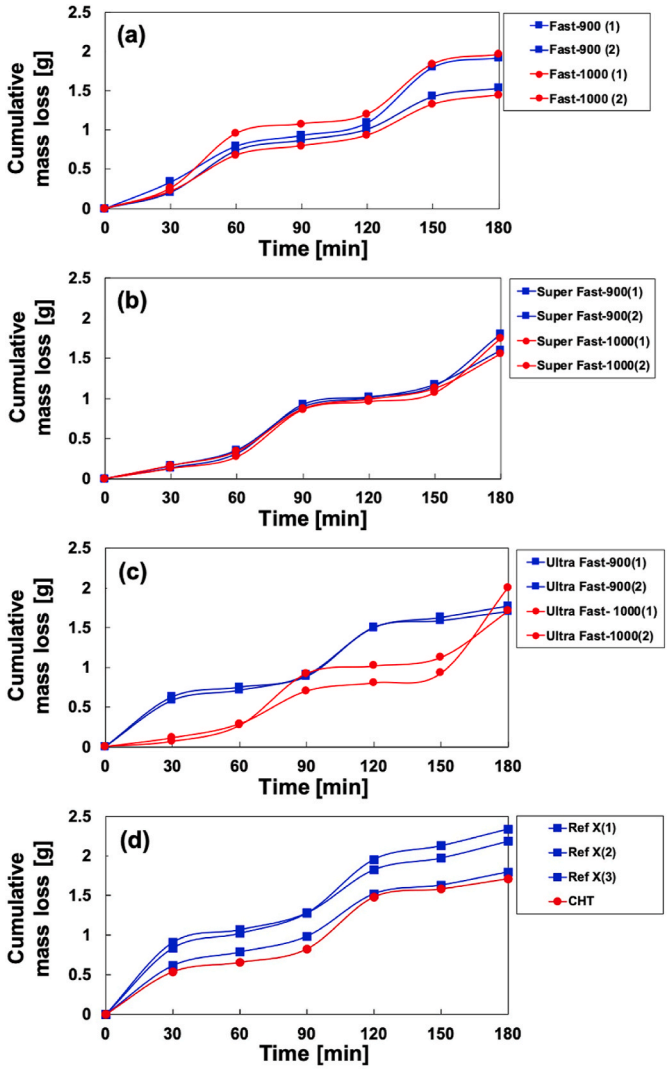

Fig. 12. The cumulative erosion which is expressed as mass loss as a function of test duration for induction hardened samples with the rate of heating of a) Fast about 50 °C/s, b) Super Fast about 100 °C/s, c) Ultra Fast about 500 °C/s, and for the d) reference materials.

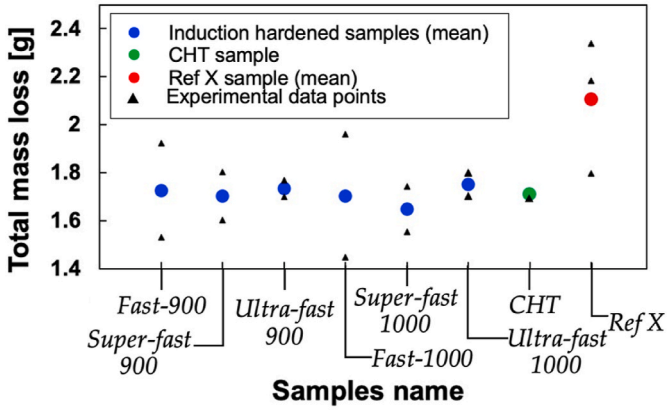

Fig. 13. Total mass loss of the samples including the mean value and experimental data points.

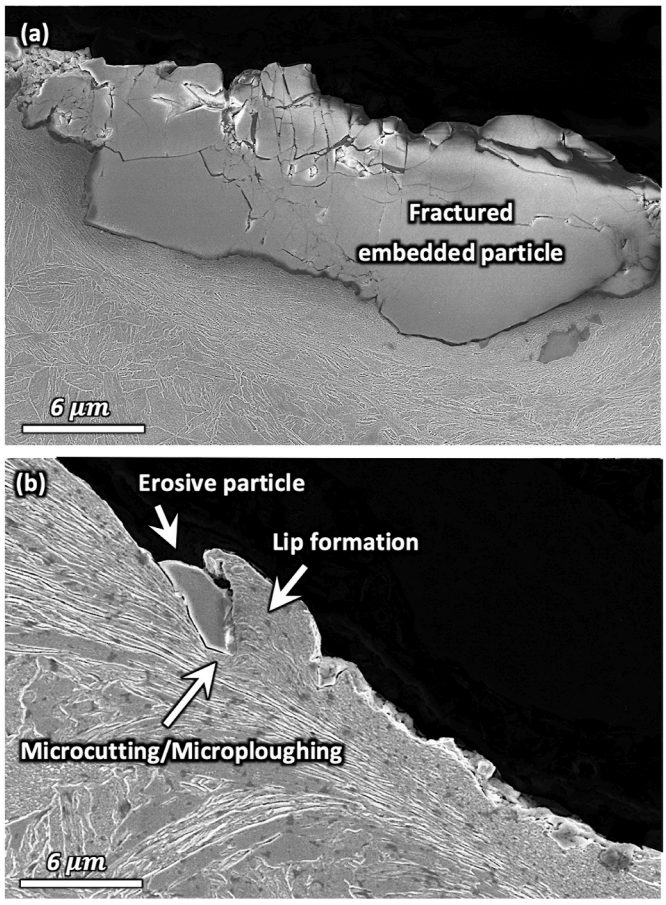

Fig. 14. a) A significant amount of material removal from the surface by a very large particle in Fast-900 sample. b) The cutting and ploughing mechanism observed in the Ultra Fast-1000 sample.

the Ultra Fast-900 sample.

In contrast to the prior austenite grain size, the difference in martensite block size amongst the studied samples was not that significant. Due to the very fine prior austenite grain structure which was observed in all the specimens and most probably due to the high amount of nucleation sites for the martensite formation, the induction hardened samples showed such similar final microstructures. Even for the Fast-1000 sample, which obtained the largest prior austenite grain structure amongst the six target samples, a fine and ultra-hard lath-type martensitic microstructure was achieved. In other words, the significant decrease in mean ECD value of the prior austenite grain size from about 15 μm to 2 μm, which has been observed here, resulted in only a slight change in the size of the martensite blocks. However, in the reference materials, large and bulky martensite blocks were observed as a result of the transformation from the large prior austenite grain structure. Hence, a maximum martensite block size of 8.20 μm, expressed as ECD value, was recorded for the CHT sample and a maximum of 13.10 μm was observed in Ref X.

Fig. 10 shows the variations of martensite block size as a function of prior austenite grain size (mean ECD values). As can be seen, in the range of austenite grain size studied here (2–15 μm), the martensite block size exhibited a slight increase from 1.5 μm to 2.5 μm. However, in the case of Ref X sample with a large prior austenite grain size (24 μm), a large martensite block size of 5.5 μm, 5 times larger than that in Ultra Fast-900, was observed. A logarithmic correlation was found to describe the relationship between the prior austenite and final martensite blocks for the studied material (Ref X was excluded from the curve fitting due to the different composition).

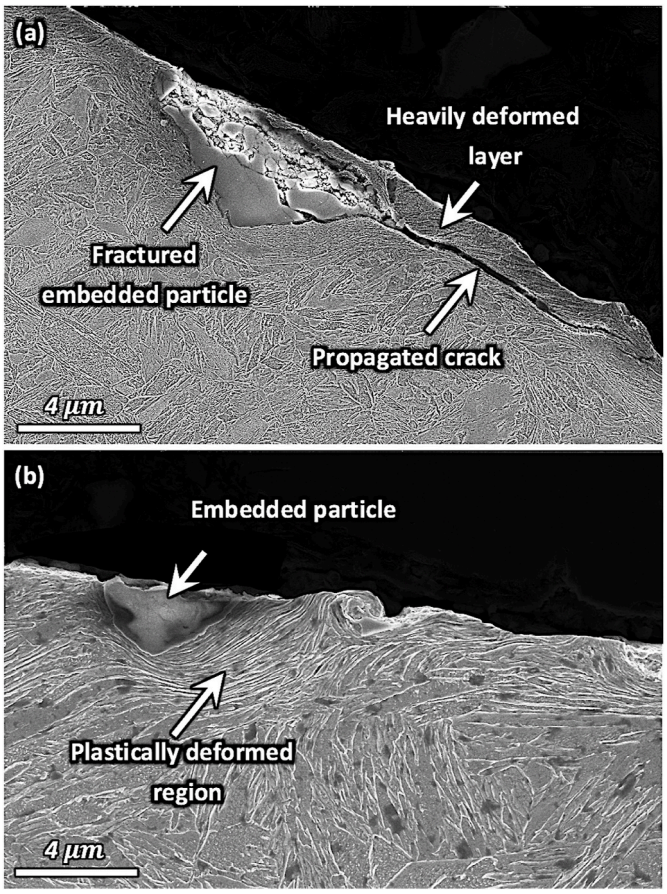

Fig. 15. a) Material removal by an embedded particle and subsequent delamination and fracture mechanism (Fast-900 sample). b) Severe deformation of the impacted surface by transferring the kinetic energy of granite particle to the surface (Super Fast-1000).

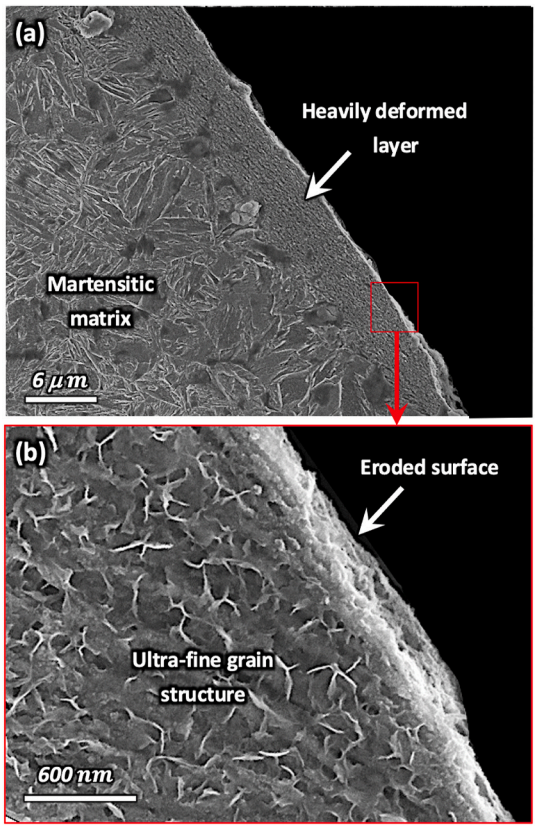

Fig. 16. A FESEM image of the heavily deformed and ultra-fine surface layer indicating the formation of cell-like structure formation by severe plastic deformation (Ultra Fast 1000).

3.2. Hardness

The hardness values of the samples prior to the erosion test are presented in Fig. 11. The hardness values of the samples after induction hardening fall in the same range for both peak temperatures, while the two reference materials, especially Ref X, showed a lower hardness level. Ref X had a notably lower carbon content and different composition, hence the lower hardness. However, comparing the hardness results of the induction hardened samples and the grain size data it can be concluded that the hardness homogeneity, as well as the grain structure uniformity, were highest with the fast heating rate (about 50 °C/s), especially for those samples which were re-austenitized at the peak temperature of 900 °C. In the case of CHT sample, the hardness value is to a certain extent lower than that of the induction hardened sample. The slightly larger martensite block size of the CHT samples may explain this minor difference in the hardness values of the studied materials. Thus, one can conclude that in the range of 2–15 μm for the prior austenite grain size, similar martensite block sizes are achieved resulting in similar hardness levels. In other words, for given carbon content, the martensite block size is the determining factor for hardness value in this range of prior austenite grain size.

3.3. Slurry erosion behavior

3.3.1. Mass loss

In erosion tests, the behavior of the samples was macroscopically quite similar. Grooves and indentations of different sizes were clearly observed on the sample surfaces for all the materials. The cumulative mass loss generated by the granite particles impingements as a function of test duration is presented in Fig. 12. The specimens were subjected to fresh slurry every 30 min, which led to a progressive weight loss by increasing the test time in all the samples. Several changes in the slope were observed in the results indicating that erosion rate depends notably on the sample position in this type of pot-tester. In the test cycles, the percentage of material removal was highest for the lowest sample position. This indicates that the number of impacts by the large particles and the concentration of the particles was higher in the lower parts of the pot than elsewhere. This effect was canceled by switching the samples between sample levels twice during the test.

The mean value of the total mass loss along with all the experimental data points are shown in Fig. 13. The total mass loss after 180 min ranged from 1.44 g (Fast-1000) to 2.34 g (Ref X) indicating that the erosion conditions were harsh in comparison to those reported elsewhere for smaller particles and lower velocities that give mass losses on the milligram scale, [30–33]. However, the differences between the heat-treated steels were minor. It should be also remarked that as some granite particles were embedded into the surface of the samples, the actual weight loss is slightly higher than the measured weight loss for all the samples. However, the embedded granite particles are very small, and generally more particles are embedded in the softer steels, which still show a much greater mass loss. Therefore, any possible effect of the abrasive embedding on the total mass loss was considered insignificant in the current tests.

3.3.2. Characterization of eroded surfaces

The eroded samples were subjected to detailed characterization using FESEM and EBSD. Some results are presented in Figs. 14 and 15. The characterization of the cross-sections revealed that several wear mechanisms were active and operative during the slurry erosion test. It

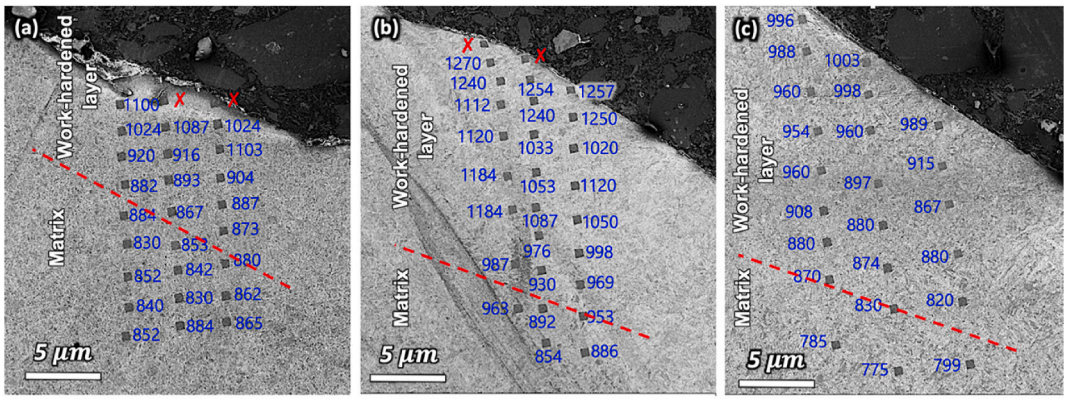

Fig. 17. The microhardness profiles below the eroded surface for a) Super Fast-900, b) Fast-1000, c) CHT samples. The hardness values are on the Vickers scale and were measured under 0.1 N load.

was found that the main mechanisms responsible for the erosion behavior of the studied steels were heavy plastic deformation and fracture, microploughing, delamination, and (micro)cutting.

In general, the high-speed slurry-pot erosion test involves chaotically traveling solid hard particles striking the target material surface at different velocities and different impact angles varying from 0 to 90°. When the impact angle is parallel to the test surface, or near 0°, the main wear mechanism is abrasion, not erosion, and damage occurs mainly due to microploughing, wedge formation, and microcutting [34]. At greater impact angles, the material surface is deformed, displaced, or removed from the place of the impact where the particle may embed through the surface depending on the impact energy. At impact angles approximately normal to the test surface, the material displacement and deformation reach a maximum, and a significant amount of material may easily be ejected from the target surface, especially by massive particles as shown in Fig. 14(a), where the size of the embedded particle is over 25 μm. Moreover, the sequence of high-speed particle impacts caused a severe deformation on the target surface which led to the work-hardening phenomena on the surface and the formation of an ultra-hard layer below the eroded surface.

In this study, two different erosion mechanisms were mainly responsible for the total erosion rate: i) for the harder samples or in the presence of hard layer, fracture, and material removal by large embedded particles with a higher hardness and ii) for the softer samples or in the absence of hard layer, extensive plastic deformation caused by microploughing. However, different erosion mechanisms typically act simultaneously depending on the kinetic energy of the particles, the impact angle, and the local characteristics of the target material like hardness and ductility. Some examples of the heavily deformed and eroded cross-sections of the surfaces are given in Figs. 14 and 15. The severity of the erosive conditions can be addressed from the close-up images of the erosive particle embedment and the orientated microstructural components as shown in both Figs. 14 and 15. Interestingly, the embedded large granite particle in Fig. 14(a) has fractured due to impinging the surface and later collisions by the other particles. The embedded particle shows very sharp corners surrounded by deformed microstructure. Despite material removal, such a sharp, hard particle might lead to crack formation, if the test were to be continued, due to the high-stress concentrations like in Fig. 15(b). An example of microcutting and microploughing having taken place is shown in Fig. 14(b), in which a piece of granite has cut steel in front of the particle resulting in lip formation. Eventually, this lip would be removed by the cutting or ploughing caused by subsequent particle impacts.

Fig. 14(b) also shows how the martensitic microconstituents in the vicinity of the surface have been deformed. Immediately below the surface, an extremely fine, almost nano-structured layer has been formed. Owing to the sequence of high-speed particle impacts, the steel surface may experience work-hardening where a narrow ultra-hard and ultra-fine structured layer is formed near the eroded surface. This layer can improve the erosion resistance of the surface thanks to its hardness level. However, due to its brittleness, it might be easily removed, at least partially, by the nucleation and propagation of sub-surface cracks [35] like in Fig. 15(a). It can be clearly seen that a crack has propagated underneath the heavily deformed surface along the boundary of the deformed and undeformed regions. The crack has presumably initiated from the embedded particle, also visible in the image next to the crack. This image evidently shows one of the material removal and fracture mechanisms taking place during slurry erosion. In the absence of the heavily deformed layer, some more ductile wear surface behavior was also noted, as shown for example in Fig. 15(b). The sample (Super Fast-1000) shows a plastically deformed martensitic microstructure elongated in the direction of the erosive particles flow. Yet, there is no clearly visible hard layer on top of the deformed surface, most probably it has been removed from the surface by the mechanism given above. A fresh, work-hardened layer would be produced if the test were to be continued due to further particle impacts.

The extremely fine, heavily deformed, and work-hardened layer near the eroded surface is shown in close-up in Fig. 16. In the FESEM image, the layer appears dark with an almost indistinguishable cell-like structure, as shown in higher magnification (Fig. 16(b)). This type of layer has been detected after harsh abrasive wear and is typical for martensitic steels [20]. It is often referred to as a white etching layer due to its white appearance in a light optical microscope.

Microhardness profiles were made on the eroded samples to measure the hardness of the deformed region and to evaluate the depth of deformation. Some examples are given in Fig. 17. It was observed that due to the work-hardening phenomenon and ultra-fine structure formation on the region near the eroded surface, the hardness was increased compared to the hardness of the matrix and undeformed region. For example, the Fast-1000 sample had hardness peaking at 1100 HV and the conventionally heat-treated CHT showed maximum microhardness of around 1000 HV. The highest measured hardness reached values greater than 1200 HV for the Super Fast-1000 sample. However, due to the difference in the grain size, different work-hardened layer thicknesses were observed. The work-hardened layer in the CHT material extended from the surface down to a depth of about 14 μm, while it was only half that for the Super Fast-900 material which had the finest grain structure. It should be noted that the bulk hardness measured with the microhardness tester is higher than that measured in macrohardness testing due to the lower applied force.

In this research work, the work-hardened, fine-structured layer closest to the eroded surface has been characterized in the greatest detail. Often the thickness of the discussed layer is relatively high, such as in Fig. 16 where the depth of the deformed layer is more than 5 μm,

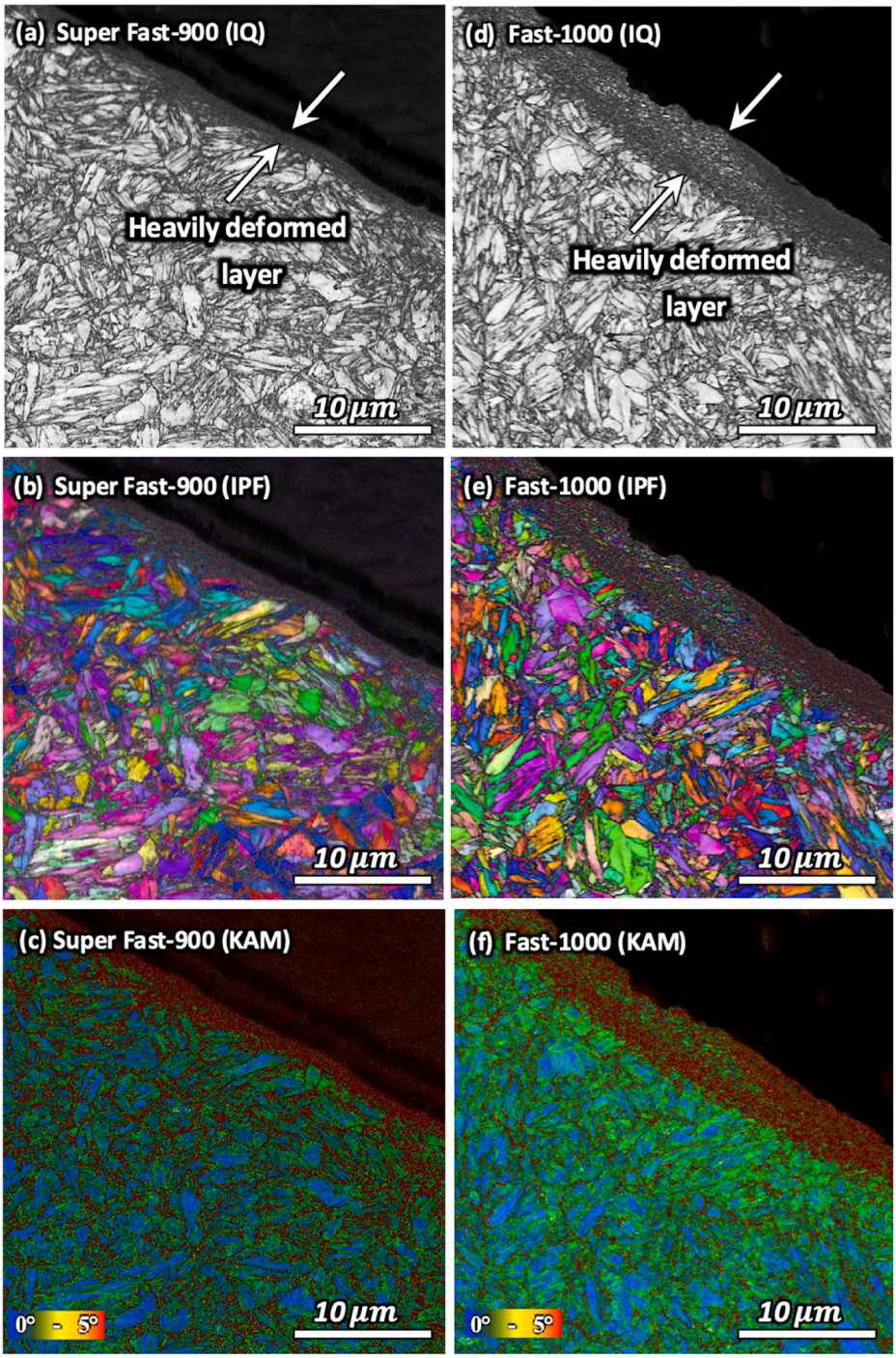

Fig. 18. a, d) Image quality (IQ), b, e) inverse pole figure (IPF), and c, f) kernel average misorientation (KAM) maps for Super Fast-900 and Fast-1000 samples.

but sometimes it is quite thin like that in Fig. 14(b). Therefore, as the properties of the deformed layer, and furthermore, the interface between the layer and the bulk structure are thought to play a significant role in determining the susceptibility to cracking and subsequent delamination, EBSD measurements were made on the regions near the eroded sample surfaces. Two sets of results are given in Fig. 18 and Fig. 19. Fig. 18 shows the results for the Ultra Fast-900 sample, which had the finest grain structure, and the Fast-1000 which had the coarsest grain structure amongst the induction treated samples. For comparison, the results of the two reference materials (CHT, Ref X) are presented in Fig. 19.

The IQ maps (Fig. 18a,d, and 19a,d) mostly consist of two distinct regions, a narrow and dark layer near the eroded surface and then slightly further a lighter and wider region. Comparing the IQ maps with inverse pole figure maps (IPF), given in Fig. 18(b,e) and 19 (b,e), and Kernel average misorientation (KAM) maps, presented in Fig. 18(c,f) and 19 (c,f), it can be concluded that the first region is associated with the heavily deformed layer with an ultrafine structure which looks darker compared to the rest of the image due to a higher fraction of grain boundaries and higher density of dislocations. As an example, the high-magnification IPF map from a Fast-1000 sample in Fig. 20 shows that the deformed layer is comprised of ultrafine grains with an average size of about 200 nm surrounded by high-angle grain boundaries. It has been explained previously [10] that the formation mechanism of these freshly

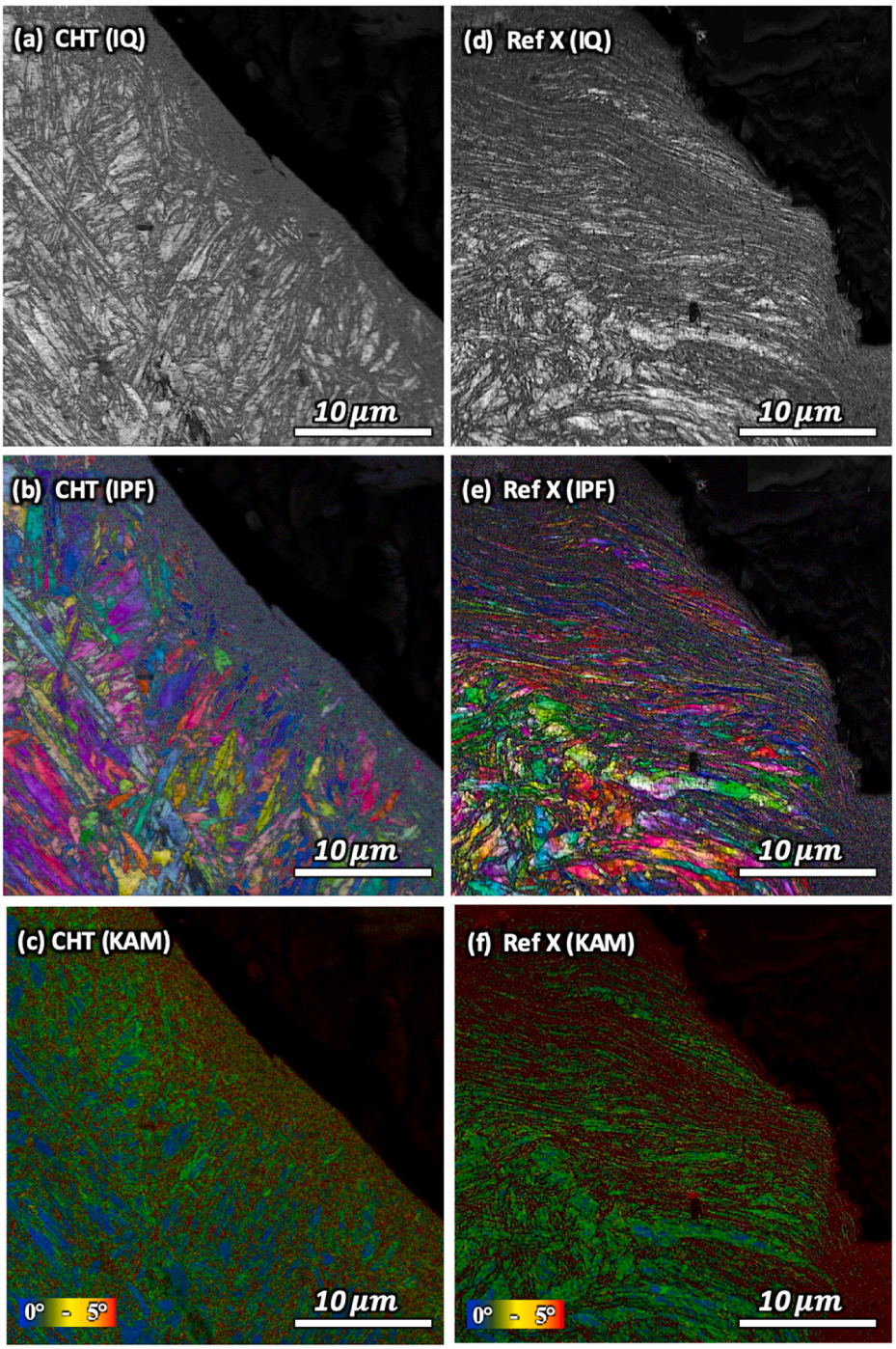

Fig. 19. a,d) Image quality (IQ), b, e) inverse pole figure (IPF) and c, f) kernel average misorientation (KAM) maps for CHT and Ref X samples.

formed grains is different from those normally formed by nucleation and growth involving grain boundary migration. According to Sakai et al. [36], the mechanism here could be a combination of fragmentation of the original grains and rearrangement of deformation bands into high-angle boundaries as a result of increasing the misorientations between the shear bands under severe repeated impingements. Similar observations of an ultrafine, dark region characterized with EBSD were made in a previous paper concerning a 500 HB grade wear-resistant steel [16].

Local Kernel average misorientation maps have been commonly used as an effective way to calculate local strain concentrations and also to present the geometrically necessary dislocation density distribution in a deformed microstructure [30–32]. Fig. 18(c,f) and 19 (c,f) show the KAM maps for Super Fast-900, Fast-1000, CHT, and Ref X samples. The color code indicates that misorientation angles range from 0° (blue) to 5° (red). Generally, misorientation angles greater than 5° are not considered in the KAM calculation as they may interfere with low-angle grain boundaries. A high amount of strain accumulation in the deformed layer is apparent, indicating work-hardening also taking place in this region. Therefore, the hardness of this thin layer is higher than that measured for the deformed layer beneath.

According to the EBSD results, the samples showed different thicknesses of the fine deformed region, as a result of differences in work-hardening capacity. The Super Fast-900 material with the smallest PAGS had a visibly thinner and finer-grained layer than the Fast-1000 sample. However, the average mass loss for nearly all the induction

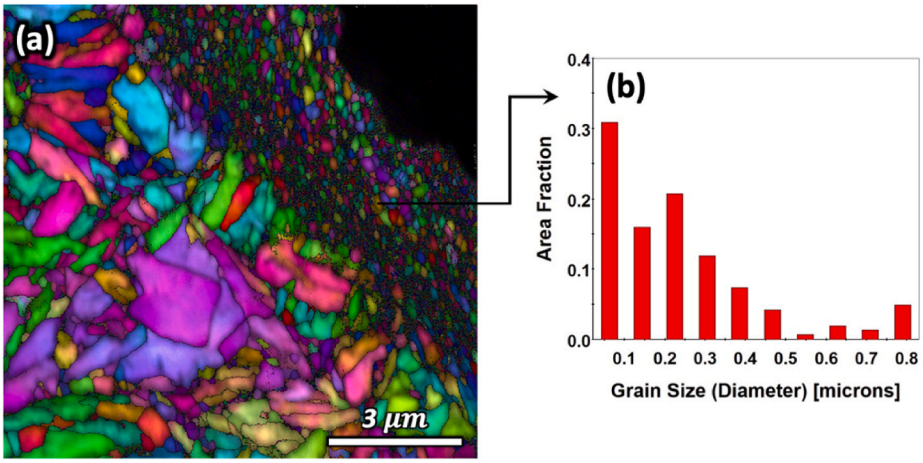

Fig. 20. a) A high magnification inverse pole figure of the eroded surface along with the overlayed high angle grain boundaries for a Fast-1000 sample indicating the ultra-fine grain formation in the heavily deformed layer and b) corresponding nanosized grain distribution.

hardened samples was within the deviation, and the two samples compared here (Super Fast-900 with 1.701 g vs Fast-1000 with 1.703 g) showed practically no difference regarding the total average mass loss in the slurry-erosion testing. This indicates that the two samples had somewhat different material removal behavior that eventually led to the almost same results regarding the mass loss. The conventionally heat-treated (CHT) sample also showed wear performance on par with the induction hardened samples despite having larger PAGS. The EBSD maps for the CHT sample are given in Fig. 19(a–c). The dark, fine-grained layer is also visible for the CHT, but the depth of the deformed region is greater compared to the induction hardened samples. Presumably, the hardness of the deformed region is not as high as the induction hardened samples showed, as the microhardness profile also showed lower hardness values (see Fig. 17). However, the deformed layer for the CHT sample shows less drastic differences in the contrast, i.e. the deformation not only reaches deeper into the bulk material but is also less severe. Therefore, the gradient between the surface and the bulk material is lower. Initially, the hardness was slightly lower, while the PAGS was somewhat larger for the CHT in comparison to the more rapidly heated and quenched induction samples. Yet, there were not that great differences in the martensite peak block size, though the size distribution was wider (see Fig. 9).

The commercial martensitic wear-resistant steel (Ref X) showed a much greater mass loss in the testing compared to the other samples, and this could be seen also in EBSD mapping. Fig. 19(c-d) show how the deformed and bent laths extend much deeper into the bulk structure. Unlike the other samples, no clear interface or heavily deformed layer is visible. Although the Ref X had much lower initial hardness, the steel is also presumably more ductile than the other steels tested that had higher carbon contents. Moreover, the wear mechanisms were different for Ref X, as more ductile behavior could be expected. The hard, high-speed abrasives had caused more ploughing of the surface, while less cracking could be seen. However, the initial hardness was much lower for Ref X, and therefore the hard particles caused higher mass loss when compared to the induction hardened steels.

The results suggest that PAGS does not have a significant role regarding the mass loss under the harsh slurry-erosive conditions applied in this work. However, the martensite block size appears to be a more important factor. It has been widely reported [18,19] that the refinement of martensite packet and block size improves fracture toughness due to the increased density of high-angle boundaries, which hinder cleavage crack propagation. Higher toughness can also result in higher resistance against the localized shearing, which is one of the main mechanisms for material removal.

Work hardening significantly changes the local characteristics of the target surface. It has been demonstrated that pearlitic steels perform better than harder martensitic alloys due to their higher work hardening capacity playing a key role in determining the wear rate [37]. The higher the work hardening capacity the higher the general toughness. On the other hand, when the ductility is higher, the work hardening capacity would be higher. Recently, Chintha et al. [34] showed in low-alloyed steels that despite the lower initial hardness, the hot rolled steel revealed a greater hardness in the vicinity of the wear surfaces after the impeller-tumbler tests compared to the quenched grade because of its greater capacity to work-hardening which results from its greater ductility. Similarly, it is also expected here that the ductility and work hardening capacity to be increased with increasing the initial austenite grain size and consequently corresponding martensite block size.

It seems that the samples with a smaller prior austenite grain and martensite block size had a better resistance against cleavage fracture, while the sample with a larger prior austenite grain size had a higher work hardening capacity producing a thicker deformed, ultra-hard surface layer. The overall effect is that both small and large prior austenite grain sizes lead to similar erosion rates. However, the future interest of the research team would transmission electron microscopy investigations for studying the role of martensitic laths and dislocations arrangement on the achieved results and also for the detailed characterization of cell-like and nano-size grain structure near the eroded surface.

4. Conclusions

The effect of prior austenite grain size and martensite block size on the slurry erosion performance of a medium-carbon, low-alloy steel has been evaluated using a high-speed slurry-pot wear tester to generate accelerated wear under harsh conditions. Induction hardening with different heating rates and different peak temperatures were used to produce martensitic microstructures with prior austenite grain sizes varying from about 2 to about 15 μm. On the basis of the present investigation and analysis the following results can be concluded:

- The finest prior austenite grain structure, which was also normally distributed and equiaxed, was achieved with a peak temperature of 900 °C and a heating rate of 500 °C/s (Super Fast-900).
- The range of prior austenite grain size achieved in this work was fine enough to produce a hard-martensitic microstructure with a hardness of about 670 HV10 after rapid quenching.
- The slurry erosion environment applied in this study was certainly aggressive that caused a material removal on the gram scale after only 180 min test duration.

- The 2–15 μm difference in prior austenite grain size resulted in only small differences in the final martensitic block sizes, i.e. 1.5–2.5 μm. However, this small difference led to different work-hardening behavior.
- No significant effect of prior austenite grain size on erosion mass loss was observed.
- Microhardness and microstructure examination of cross-sections after erosion testing revealed that a finer prior austenite grain size led to lower work hardening capacity, which presumably canceled the expected beneficial effect of austenite grain size on cleavage fracture resistance, thereby explaining the lack of any detectable effect of prior austenite grain size on erosion performance.
- High magnification EBSD imaging revealed that the severe plastic deformation caused by the sequence of large particle impacts on the surface created an ultra-fine, ultra-hard surface layer, the hardness of which reached about 1270 HV in the sample heated at 50 °C/s to 1000 °C.

Data availability

The raw/processed data required to reproduce these findings cannot be shared at this time as the data also forms part of an ongoing study but will be made available on request.

Credit authorship contribution statement

Vahid Javaheri: Writing - original draft, Formal analysis, Investigation, Resources, Visualization, Data curation, Conceptualization. **Oskari Haiko:** Writing - original draft, Formal analysis, Data curation. **Saeed Sadeghpour:** Writing - original draft, Formal analysis, Investigations, Data curation, Visualization. **Kati Valtonen:** Review & editing. **Jukka Kömi:** Project administration, Supervision. **David Porter:** Conceptualization, Review & editing, Supervision.

Declaration of competing interest

The authors declare that they have no known competing financial interests or personal relationships that could have appeared to influence the work reported in this paper.

Acknowledgment

The authors are grateful for the financial support from the Academy of Finland (#311934 – Genome of Steel Project). The corresponding author would also like to thank Jenny and Antti Wihuri Foundation for the financial support.

References

[1] H. Arabnejad, A. Mansouri, S.A. Shirazi, B.S. McLaury, Development of mechanistic erosion equation for solid particles, Wear 332–333 (2015) 1044–1050, https://doi.org/10.1016/j.wear.2015.01.031.
[2] H.H. Tian, G.R. Addie, K.V. Pagalthivarthi, Determination of wear coefficients for erosive wear prediction through Coriolis wear testing, Wear 259 (2005) 160–170, https://doi.org/10.1016/j.wear.2005.02.097.
[3] L. Ma, C. Huang, Y. Xie, J. Jiang, K.Y. Tufa, R. Hui, Z.S. Liu, Modeling of erodent particle trajectories in slurry flow, Wear 334–335 (2015) 49–55, https://doi.org/10.1016/j.wear.2015.04.013.
[4] Y.F. Wang, Z.G. Yang, Finite element model of erosive wear on ductile and brittle materials, Wear 265 (2008) 871–878, https://doi.org/10.1016/j.wear.2008.01.014.
[5] V. Javaheri, D. Porter, V.-T. Kuokkala, Slurry erosion of steel – review of tests, mechanisms, and materials, Wear 408–409 (2018) 248–273, https://doi.org/10.1016/j.wear.2018.05.010.
[6] R. Gupta, S.N. Singh, V. Sehadri, Prediction of uneven wear in a slurry pipeline on the basis of measurements in a pot tester, Wear 184 (1995) 169–178, https://doi.org/10.1016/0043-1648(94)06566-7.
[7] H.M. Clark, R. Llewellyn, Assessment of the erosion resistance of steels used for slurry handling and transport in mineral processing applications, Wear 250 (2001) 32–44, https://doi.org/10.1016/S0043-1648(01)00628-7.
[8] N.R. Steward, The Wear of Materials in Hydraulic Transport Pipelines, Cape town, 1988.
[9] T. Alam, M. Aminul Islam, Z.N. Farhat, Slurry erosion of pipeline steel: effect of velocity and microstructure, J. Tribol. 138 (2015), 021604, https://doi.org/10.1115/1.4031599.
[10] T. Alam, Z.N. Farhat, Slurry erosion surface damage under normal impact for pipeline steels, Eng. Fail. Anal. 90 (2018) 116–128, https://doi.org/10.1016/j.engfailanal.2018.03.019.
[11] B.K. Gandhi, S.N. Singh, V. Seshadri, Study of the parametric dependence of erosion wear for the parallel flow of solid-liquid mixtures, Tribol. Int. 32 (1999) 275–282, https://doi.org/10.1016/S0301-679X(99)00047-X.
[12] E.O. Hall, The deformation and ageing of mild steel: III discussion of results, Proc. Phys. Soc. B 64 (1951) 747–753, https://doi.org/10.1088/0370-1301/64/9/303.
[13] N.J. Petch, The cleavage strength of polycrystals, Journal of Iron and Steel Institute, J. Iron Steel Inst. 174 (1953) 25–28.
[14] C. Wang, M. Wang, J. Shi, W. Hui, H. Dong, Effect of microstructural refinement on the toughness of low carbon martensitic steel, Scripta Mater. 58 (2008) 492–495, https://doi.org/10.1016/j.scriptamat.2007.10.053.
[15] C. Zhang, Q. Wang, J. Ren, R. Li, M. Wang, F. Zhang, K. Sun, Effect of martensitic morphology on mechanical properties of an as-quenched and tempered 25CrMo48V steel, Mater. Sci. Eng. 534 (2012) 339–346, https://doi.org/10.1016/j.msea.2011.11.078.
[16] O. Haiko, V. Javaheri, K. Valtonen, A. Kaijalainen, J. Hannula, J. Kömi, Effect of prior austenite grain size on the abrasive wear resistance of ultra-high strength martensitic steels, Wear 454–455 (2020) 203336, https://doi.org/10.1016/j.wear.2020.203336.
[17] A.R. Chintha, Metallurgical aspects of steels designed to resist abrasion, and impact-abrasion wear, Mater. Sci. Technol. 35 (2019) 1133–1148, https://doi.org/10.1080/02670836.2019.1615669.
[18] V. Javaheri, S. Kolli, B. Grande, D. Porter, Insight into the induction hardening behavior of a new 0.40% C microalloyed steel: effects of initial microstructure and thermal cycles, Mater. Char. 149 (2019) 165–183, https://doi.org/10.1016/j.matchar.2019.01.029.
[19] V. Javaheri, N. Khodaie, A. Kaijalainen, D. Porter, Effect of niobium and phase transformation temperature on the microstructure and texture of a novel 0.40% C thermomechanically processed steel, Mater. Char. 142 (2018) 295–308, https://doi.org/10.1016/j.matchar.2018.05.056.
[20] V. Javaheri, A. Pohjonen, J.I. Asperheim, D. Ivanov, D. Porter, Physically based modeling, characterization and design of an induction hardening process for a new slurry pipeline steel, Mater. Des. 182 (2019) 108047, https://doi.org/10.1016/j.matdes.2019.108047.
[21] V. Javaheri, S. Pallaspuro, A. Kaijalainen, S. Sadeghpour, J. Kömi, D. Porter, Promising bending properties of a new as-rolled medium-carbon steel achieved with furnace-cooled bainitic microstructures, Mater. Sci. Eng. 796 (2020) 140011, https://doi.org/10.1016/j.msea.2020.140011.
[22] N. Ojala, K. Valtonen, P. Kivikytö-Reponen, P. Vuorinen, P. Siitonen, V.-T. Kuokkala, Effect of test parameters on large particle high speed slurry erosion testing, Tribol. Mater. Surface Interfac. 8 (2014) 98–104, https://doi.org/10.1179/1751584X14Y.0000000066.
[23] N. Ojala, K. Valtonen, A. Antikainen, A. Kemppainen, J. Minkkinen, O. Oja, V. Kuokkala, Wear performance of quenched wear resistant steels in abrasive slurry erosion, Wear 354–355 (2016) 21–31, https://doi.org/10.1016/j.wear.2016.02.019.
[24] N. Ojala, K. Valtonen, J. Minkkinen, V.T. Kuokkala, Edge and particle embedment effects in low- and high-stress slurry erosion wear of steels and elastomers, Wear 388–389 (2017) 126–135, https://doi.org/10.1016/j.wear.2017.06.004.
[25] K. Valtonen, N. Ojala, O. Haiko, V. Kuokkala, Comparison of various high-stress wear conditions and wear performance of martensitic steels, Wear (2019) 426–427, https://doi.org/10.1016/j.wear.2018.12.006.
[26] T. Nyyssönen, M. Isakov, P. Peura, V.-T. Kuokkala, Iterative determination of the orientation relationship between austenite and martensite from a large amount of grain pair misorientations, Metall. Mater. Trans. 47 (2016) 2587–2590, https://doi.org/10.1007/s11661-016-3462-2.
[27] G. Kurdjumow, G. Sachs, Uber den mechanismus der Stahlhärtung, Zeitschrift Fur Phys 64 (1930) 325–343, https://doi.org/10.1007/BF01397346.
[28] V. Javaheri, T. Nyyssönen, B. Grande, D. Porter, Computational design of a novel medium-carbon, low-alloy steel microalloyed with niobium, J. Mater. Eng. Perform. 27 (2018) 2978–2992, https://doi.org/10.1007/s11665-018-3376-9.
[29] S. Morito, X. Huang, T. Furuhara, T. Maki, N. Hansen, The morphology and crystallography of lath martensite in alloy steels, Acta Mater. 54 (2006) 5323–5331, https://doi.org/10.1016/j.actamat.2006.07.009.
[30] M. Lindgren, J. Perolainen, Slurry pot investigation of the influence of erodent characteristics on the erosion resistance of austenitic and duplex stainless steel grades, Wear 319 (2014) 38–48, https://doi.org/10.1016/j.wear.2014.07.006.
[31] A. Jafari, K. Dehghani, K. Bahaaddini, R. Abbasi, Experimental comparison of abrasive and erosive wear characteristics of four wear-resistant steels, Wear 416–417 (2018) 14–26, https://doi.org/10.1016/j.wear.2018.09.010.
[32] T.J. Harvey, J.A. Wharton, R.J.K. Wood, Development of synergy model for erosion–corrosion of carbon steel in a slurry pot, Tribol. Mater. Surface Interfac. 1 (2007) 33–47, https://doi.org/10.1179/175158407X181471.
[33] G.R. Desale, B.K. Gandhi, S.C. Jain, Improvement in the design of a pot tester to simulate erosion wear due to solid – liquid mixture, Wear 259 (2005) 196–202, https://doi.org/10.1016/j.wear.2005.02.068.
[34] A.R. Chintha, K. Valtonen, V. Kuokkala, S. Kundu, M.J. Peet, H.K.D.H. Bhadeshia, Role of Fracture Toughness in Impact-Abrasion Wear, 2019.

[35] Y.Y. Yang, H.S. Fang, W.G. Huang, A study on wear resistance of the white layer, Tribol. Int. 29 (1996) 425–428, https://doi.org/10.1016/0301-679X(95)00099-.
[36] T. Sakai, H. Miura, X. Yang, Ultrafine grain formation in face centered cubic metals during severe plastic deformation, Mater. Sci. Eng. 499 (2009) 2–6, https://doi.org/10.1016/j.msea.2007.11.098.
[37] I.M. Hutchings, Wear-resistant materials: into the next century, Mater. Sci. Eng. 184 (1994) 185–195, https://doi.org/10.1016/0921-5093(94)91031-6.